Annales
Geophysicae
Open Access

# Exospheric hydrogen density distributions for equinox and summer solstice observed with TWINS1/2 during solar minimum

**J. H. Zoennchen, U. Nass, and H. J. Fahr**

Argelander Institut für Astronomie, Astrophysics Department, University of Bonn, Auf dem Huegel 71, 53121 Bonn, Germany

*Correspondence to:* J. H. Zoennchen (zoenn@astro.uni-bonn.de)

**Abstract.** The Lyman-$\alpha$ Detectors (LAD) on board the two TWINS 1/2-satellites allow for the simultaneous stereo imaging of the resonant emission glow of the H-geocorona from very different orbital positions. Terrestrial exospheric atomic hydrogen (H) resonantly scatters solar Lyman-$\alpha$ (121.567 nm) radiation. During the past solar minimum, relevant solar parameters that influence these emissions were quite stable. Here, we use simultaneous LAD1/2-observations from TWINS1 and TWINS2 between June 2008 and June 2010 to study seasonal variations in the H-geocorona. Data are combined to produce two datasets containing (summer) solstice and (combined spring and fall) equinox emissions. In the range from 3 to 10 Earth radii ($R_E$), a three-dimensional (3-D) mathematical model is used that allows for density asymmetries in longitude and latitude. At lower geocentric distances ($< 3\,R_E$), a best fitting $r$-dependent (Chamberlain, 1963)-like model is adapted to enable extrapolation of our information to lower heights. We find that dawn and dusk H-geocoronal densities differ by up to a factor of 1.3 with higher densities on the dawn side. Also, noon densities are greater by up to a factor of 2 compared to the dawn and dusk densities. The density profiles are aligned well with the Earth–Sun line and there are clear density depletions over both poles that show additional seasonal effects. These solstice and equinox empirical fits can be used to determine H-geocoronal densities for any day of the year for solar minimum conditions.

**Keywords.** Atmospheric composition and structure (Airglow and aurora; Pressure, density, and temperature) – Meteorology and atmospheric dynamics (Thermospheric dynamics)

## 1 Introduction

The determination of the 3-D shape and density structure of the terrestrial atomic neutral H-exosphere is an important research aim of the TWINS mission (**T**wo **W**ide-angle **I**maging **N**eutral-atom **S**pectrometers) (McComas et al., 2009) with maximum spacecraft altitudes of about 7.2 $R_E$. Therefore, both of the two TWINS satellites are equipped with 2 Lyman-$\alpha$ detectors (121.67 nm), which continuously measure the resonantly backscattered solar Lyman-$\alpha$ radiation of the exospheric hydrogen along a line of sight (LOS). This resonantly scattered Lyman-$\alpha$ glow is the terrestrial neutral H-geocorona. Since the outermost atmospheric layers are optically thin for this Lyman-$\alpha$ scattering process, the neutral H-column density along a line of sight is directly proportional to its measured Lyman-$\alpha$-intensity. For geocentric distances $< 3\,R_E$, however, the neutral H-geocorona turns to be optically thick.

Since the earliest measurements of the resonantly scattered Lyman-$\alpha$ radiation from the exosphere based on high altitude rocket experiments and satellites (Kupperian et al., 1959; Carruthers et al., 1976), different numerical density models of the exospheric hydrogen distribution have been developed (e.g. Johnson, 1961; Chamberlain, 1963; Thomas and Bohlin, 1972; Fahr and Shizgal, 1983; Rairden et al., 1986; Bishop, 1991; Hodges, 1994; Østgaard et al., 2003).

The TWINS1/2 spacecraft provide data from 4 separate Lyman-$\alpha$ detectors mounted on the two different satellites, which are simultaneously and continuously observing the exospheric Lyman-$\alpha$ glow. As a result the spatial coverage of the TWINS1/2 data opens up new possibilities to determine the exospheric 3-D H-density structure. Earlier TWINS1 data studies resulted in H-density profiles revealing the 3-D

H-density structures of the H-geocorona between June and September 2008 and can be found in Zoennchen et al. (2011, 2010) and Bailey and Gruntman (2011).

Very different from the earlier TWINS1 results, this work is now based on both TWINS1 and TWIN2 data from an extended period between June 2008 and June 2010. The data used are partly observed simultaneously by both TWINS1/2 satellites. The aim of this analysis was the determination of two separate exospheric hydrogen models for equinox and summer solstice under solar minimum conditions. The usage of line of sight Lyman-$\alpha$ measurements of both TWINS1/2 satellites substantially increased the exospheric coverage, because both TWINS satellites are observing the same H-geocorona from very different orbital positions with different lines of sight. The improved coverage is of critical importance to fit more reliable global H-density distribution for one single seasonal day (i.e. summer solstice and equinox).

The mathematical model used in this work is based on a tomographic enfolding of the line of sight measurements aiming at a data fit by coefficients of a spherical harmonic expansion (Zoennchen, 2006; Zoennchen et al., 2010; Nass et al., 2006; Bailey and Gruntman, 2011) without restricting assumptions for specific (i.e. angle) symmetries.

## 2   Approach

The measured Lyman-$\alpha$ intensity is the sum of the geocoronal and the interplanetary Lyman-$\alpha$ glow. With respect to the geocentric Earth intersection distances of the LAD-lines of sight, the interplanetary glow usually accounts for 10–50 percent of the measured intensities. To reduce the interplanetary part we subtract all daily calculated sky maps of the interplanetary Lyman-$\alpha$ glow based on a "hot-model" (see Sect. 12).

Between June 2008 and June 2010, the Sun had a relatively stationary Lyman-$\alpha$ emission at a very low activity level. For the seasonal H-density analysis, two separate seasonal TWINS1/2 datasets were created: The summer-solstice dataset includes TWINS1/2 data from the two solar summer solstices of 2008 and 2010 (see Fig. 1). The equinox dataset includes TWINS1/2 data from all of the solar equinox seasons between fall 2008 and spring 2010 (see Fig. 3). The fall- and spring equinox are assumed to lead to similar exospheric hydrogen density distributions under the assumption of nearly identical solar activity conditions, because both equinox seasons have the same solar tilt angle with respect to the Earth Equator of 0°. More details of the two datasets are described in Sects. 5 and 6.

In order to avoid possible solar contamination, all measurements with a solar zenith angle ≤ 90° of the detectors LOS were excluded. Unfortunately, this solar stray light effect particularly reduces the number of valid dayside measurements. In our calculations we assume single scattering under optically thin conditions, which is not a viable assump-

tion below 3 $R_{\mathrm{E}}$. Therefore, measurements with the Earth-intersection distance ($r_{\mathrm{E.i.d.}}$) $r_{\mathrm{E.i.d.}} < 3 R_{\mathrm{E}}$ are excluded. Additionally, we exclude all measurements where the line of sight intersects the Earth shadow (treated as a cylinder with 1.2 $R_{\mathrm{E}}$ radius).

The model fits in this work represent the time-invariant neutral exospheric H density distributions for the two seasons summer solstice and equinox under solar minimum conditions and thus allow the study of seasonal structural differences.

A description of the resonant Lyman-$\alpha$ scattering process within the neutral exosphere, the method of enfolding the line of sight integrated TWINS-LAD data into a 3-D neutral H density distribution and details about the TWINS-LAD instrument can be found in Zoennchen (2006), Nass et al. (2006), Zoennchen et al. (2010), and Bailey and Gruntman (2011).

## 3   Coordinate system

As described in Zoennchen et al. (2011), we use standard GSE-coordinates to fit the neutral exospheric hydrogen distribution with the geocentric distance $r$ in $R_{\mathrm{E}}$. The x–y-plane is equal to the ecliptic plane, the z-axis points towards the ecliptic north pole. The longitudinal angle $\phi$ is counted from 0° (solar direction) counter clockwise to 360° (with 180° at the antisolar direction). The latitudinal angle $\theta$ is counted from the z-axis (0° at the ecliptic north pole) to 180° (at the ecliptic south pole).

## 4   Observational coverage

The observational coverage of the circumterrestrial exospheric space is of critical importance for the quality of a global exospheric hydrogen distribution fit. Particularly the combination of TWINS1/2-data from different years (2008–2010) provide a significantly improved exospheric coverage compared to earlier TWINS Lyman-$\alpha$ analyses. The spatial coverage is increasing when the TWINS satellites observe the H-geocorona at the same seasonal day from very different orbital positions (see Figs. 1 and 3). There is a longitudinal apogee drift of both TWINS of about 3–4° per month, which is responsible for the fact that TWINS1 sees the summer-solstice H-geocorona in 2010 from a roughly 80–90° different apogee longitude, compared to 2008. Over 2 years that orbital drift allows for the observation of very different angular regions of the same seasonal geocoronal situation and improves the spatial coverage.

We assume an identical H-geocorona for the same seasonal days in different years as long as the solar activity does not change (the case between mid-2008 and mid-2010). In that context, "same seasonal day" means all days of the year with the same tilt angle of the Earth–Sun line against the Earth Equator. This assumption allows the combined fit
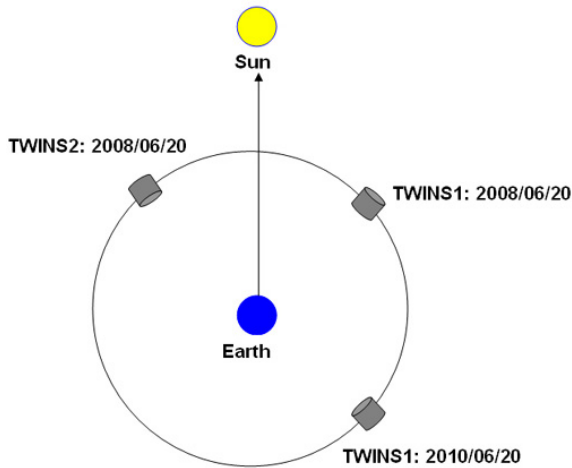
**Fig. 1.** Spacecraft positions: The TWINS1/2-apogee positions (grey cylinders) included in the summer-solstice dataset, which is combined from TWINS1/2 2008 and TWINS1 2010 summer-solstice measurements.

of TWINS1/2 data of the same seasonal days from different years.

## 5 The summer solstice dataset

In assembling the summer-solstice dataset, we used TWINS1/2 LAD1/2 stereo data from 20 June 2008 and TWINS1 LAD1/2 data from 20 June 2010. These are the days of the solar summer-solstice conditions in 2008 and 2010; therefore, this combined dataset represents the typical "summer-solstice" seasonal day in that sense.

Figure 1 shows the longitudinal apogee positions of the TWINS1/2 spacecraft relative to the solar direction of all observations in the summer-solstice dataset. It contains LAD1/2 observations taken from 3 different TWINS1/2 apogee positions relative to the solar direction and has about 52 000 lines of sight in total.

Figure 2 gives an estimate of the observational coverage quality in the summer-solstice dataset. Lines of sight intersections with the ecliptic plane (top) and the polar meridional plane (bottom), respectively, are plotted (each plane within an angluar extent of $\pm 25°$ in GSE latitude, respectively, in GSE longitude). In the ecliptic plane, the dusk region and the region just prior to dawn are the best covered. At the dayside between dawn and dusk, the coverage in longitude is roughly complete between 3–5 $R_\mathrm{E}$. The dayside long-distance lines of sight are missing, because they were mostly removed (avoided regions) due to solar stray light. In the polar meridional–plane figure it is apparent that the Northern Hemisphere is far better covered than the Southern Hemisphere.
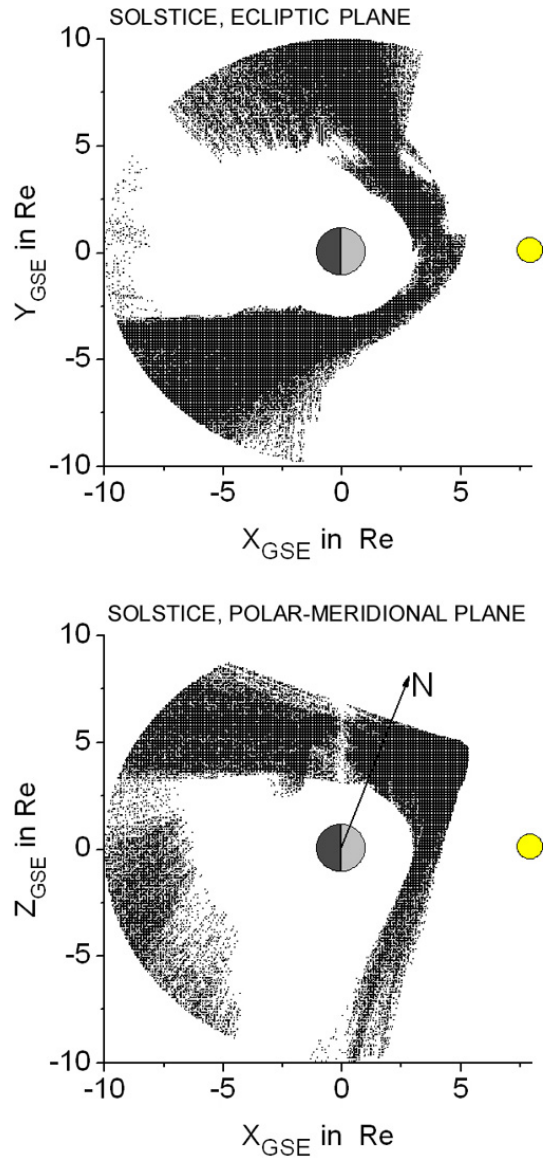


**Fig. 2.** Observational LOS-coverage: Lines of sight intersections with (top) the ecliptic plane (within an angular extent of $\theta \pm 25°$ around the ecliptic plane) and (bottom) the polar–meridonal plane (within an angular extent of $\phi \pm 25°$ around the polar–meridional plane) for the summer-solstice dataset.

## 6 The equinox dataset

Different from the yearly summer-solstice season, the solar equinox constellation returns within half a year (spring- and fall equinox). That introduces the possibility to combine spring- and fall-equinox data to one equinox dataset. In detail fall observations of 20 September 2008 (TWINS2), 20 September 2009 (TWINS2) and spring observations of 21 March 2009 (TWINS2), 21 March 2010 (TWINS1), respectively, were used to assemble the equinox dataset. Additionally, fall-equinox-near TWINS1 LAD1/2-data of the
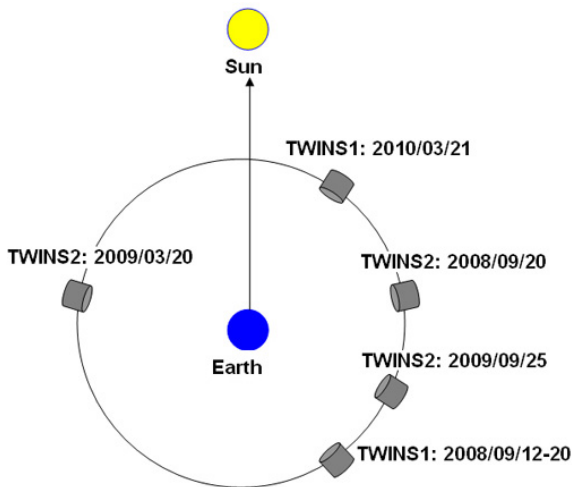
**Fig. 3.** Spacecraft positions: The TWINS1/2-apogee positions (grey cylinders) included in the equinox dataset, which was combined from TWINS1/2 measurements of different solar spring- and fall-equinox constellations between 2008 and 2010.

days 12–20 September 2008 were used, since there are unfortunately not enough valid TWINS1 LAD1/2-data around the fall-equinox day in 2008.

Figure 3 shows the longitudinal apogee positions of the TWINS1/2-spacecraft relative to the solar direction of all observations in the equinox dataset. As visible from Fig. 3, the seasonal equinox situation also is well represented by both TWINS spacecraft observing the H-geocorona from very different (apogee) positions. The equinox dataset contains about 71 500 lines of sight.

Figure 4 shows the observational coverage quality of the equinox dataset in the ecliptic and the polar meridional plane, respectively, using the same LOS-intersection conditions as in Fig. 2. In the ecliptic region the coverage here is longitudinally more complete than for the solstice dataset. Particularly the dayside has a better coverage, but the dayside LOS with intersection distances $> 5.5\,R_{\mathrm{E}}$ are also missing (avoidance region due to solar stray light). In the polar meridional region the coverage is comparable to the solstice dataset with a better coverage in the Northern than the Southern Hemisphere.

## 7   Data selection and processing

The combined seasonal days of TWINS1/2 LAD observations between 2008 and 2010 within the summer solstice dataset and the equinox dataset, respectively, are listed in Table 1.

The procedure to mark and exclude "invalid" data from the analysis was done following identical rules as described in Zoennchen et al. (2011). That means, for example, that lines of sight with an Earth-shadow intersection or those taken dur-
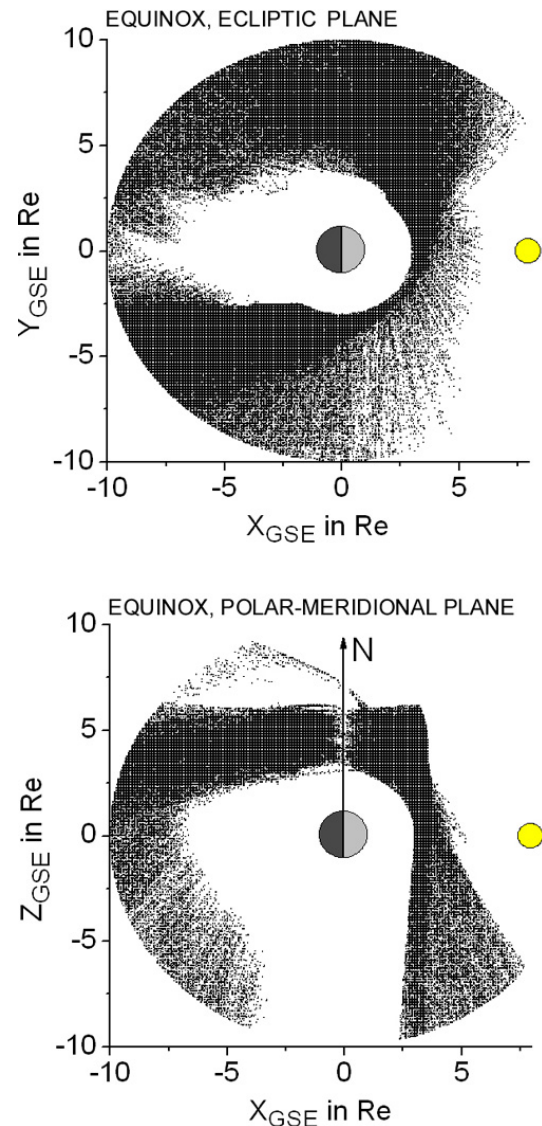




**Fig. 4.** Observational LOS-coverage: Lines of sight intersections with (top) the ecliptic plane (within an angular extent of $\theta \pm 25°$ around the ecliptic plane) and (bottom) the polar–meridonal plane (within an angular extent of $\phi \pm 25°$ around the polar–meridional plane) for the equinox dataset.

ing invalid spacecraft operation times are removed. Furthermore, a minimal geocentric Earth intersection distance for every valid line of sight of $\geq 3\,R_{\mathrm{E}}$ is required to fulfill the optically thin condition for the single scattering approximation. Finally, lines of sight with an intersection of a Lyman-$\alpha$ bright star of the galaxy are removed from the selection.

We obtained the solar Lyman-$\alpha$ line-center flux from the total solar Lyman-$\alpha$ flux as taken from SORCE SOLSTICE (see Sect. 11 and Fig. 6), adjusted by a factor resulting from the formula given by Emerich et al. (2005). The correction of the interplanetary Lyman-$\alpha$ background radiation is described in Sect. 12. For solar zenith angles $> 90°$, the
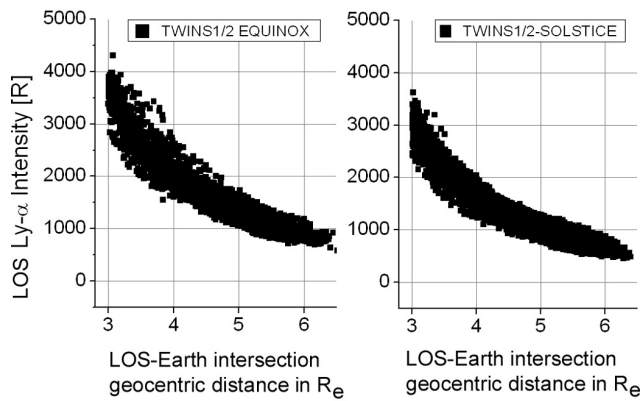
**Fig. 5.** TWINS1/2 equinox dataset (left) and summer-solstice dataset (right) LAD1/2 Lyman-$\alpha$ all lines of sight (LOS) intensities in Rayleigh [R] (recalibrated as described in Sect. 9 and interplanetary background corrected) plotted against their geocentric LOS–Earth intersection distances in $R_E$.

geocoronal attenuation of the solar Lyman-$\alpha$ flux was corrected in a similar way as practiced by Østgaard et al. (2003). All other corrections (e.g. Earth albedo Lyman-$\alpha$ glow, bright star removements and neutralized subsonic solar wind protons) were done as described in Zoennchen et al. (2010).

Figure 5 shows the Lyman-$\alpha$ intensities (recalibrated and interplanetary background corrected) against the Earth intersection distances in $R_E$ of all TWINS1/2 LAD1/2 lines of sight collected in the datasets of equinox (left) and summer solstice (right).

## 8 LAD-sensor relative calibration

Both of the TWINS1/2 spacecraft are equipped with two LAD-sensors each, which are mounted on an actuator platform. This platform permanently rotates 180° forward and 180° backward during the mission. Caused by this actuator's rotation cycle, each LAD-sensor covers a 180° half circle of the sky with a field of view angle of 4°. The 180° rotation in one direction takes roughly 90 s.

At the start-point and the end-point (turning points) of the actuator's half circle rotations, the lines of sight of both LAD1/2 sensors are (nearly) overlapping and pointing more or less in the same direction. That means that LAD1 and LAD2 are looking into the same direction in the sky with a time difference of 90 s. These two turning points (where the actuator changes its rotation direction) can be used for the determination of the relative in-flight calibration factor $f_{rel} = I_{LAD1}/I_{LAD2}$ particularly close to the apogee positions, where the spacecraft are moving relatively slowly (Zoennchen, 2006).

Ideally, the relative calibration factor $f_{rel}$ between the two LAD sensors on a TWINS satellite is expected to be always at the value of 1. Essentially, both LADs should see simi-

**Table 1.** Measured, relative calibration factors $f_{rel} = I_{LAD1}/I_{LAD2}$ at the actuator's turning points of both LADs for TWINS1/2 and different years.

| Date | TWINS1 $f_{rel}$ | TWINS2 $f_{rel}$ |
|------|------------------|------------------|
| 20 Jun 2008 | 1.01 | 1.701 |
| 20 Sep 2008 | 0.99 | 1.005 |
| 20 Mar 2009 | – | 0.854 |
| 20 Sep 2009 | – | 0.990 |
| 20 Mar 2010 | 0.650 | – |
| 20 Jun 2010 | 0.750 | – |

lar Lyman-$\alpha$ intensities coming from the same region in the sky at the actuator's turning points. However, the analysis of the TWINS1/2 data clearly shows a remarkable deviation from $f_{rel} \approx 1$ over time (see Table 1). This can be explained with a time dependent (absolute) sensitivity of one or both LAD-sensors (detectors, filters, etc.). The reason for that LAD-sensitivity change (which seems to occur individually for each LAD) is unclear so far. Nevertheless, its existence makes it unavoidable to recalibrate the absolute effectivity factors of all LADs in order to be able to transform the LAD-measurements from counts/s to usable physical units like Rayleigh [R] (for the procedure see the following Sect. 9).

Between June–September 2008, TWINS1 is very close to its ideal value for the LAD1/LAD2 relative calibration factor $f_{rel} \approx 1$ (see Table 1). Therefore, we can assume that both of the TWINS1 LAD sensors do not need a recalibration during that period. However, TWINS1 data of 2010 are showing values of $f_{rel} \approx 0.65$ (spring 2010) and $f_{rel} \approx 0.75$ (summer 2010). This is a clear deviation from $f_{rel} \approx 1$ and those TWINS1 data therefore need an absolute recalibration.

The TWINS2 LAD-sensors started in June 2008 with a relative calibration factor of $f_{rel} = 1.7$, remarkably different from its ideal value of 1. Later, the relative calibration factor came down to values between 0.85 und 1.0. Therefore, TWINS2 data need an absolute recalibration from the very beginning. The initial deviation of the TWINS2 LAD sensors from its ideal relative calibration value of 1 is not explained yet but may have occured during the storage period of over 5 years by some unknown effects of the spacecraft on ground before launch.

## 9 LAD-sensor absolute recalibration

Both TWINS1/2 spacecraft do not provide a direct facility for an in-flight recalibration of the absolute LAD sensitivity. Therefore, an indirect method is needed to quantify this absolute LAD sensitivity factors in flight. Important for any method is the existence of a (assumed to be) stable source of Lyman-$\alpha$ radiation with a well-known Lyman-$\alpha$ intensity inside the sensitivity range of the LAD-sensors. In the

**Table 2.** TWINS1-LAD (absolute and relative $f_{\mathrm{rel,recal}}$) effectivity calibration factors, newly calibrated for 2010.

| Date | TWINS1 $\eta_{\mathrm{LAD1}}$ Abs. calfactor cts/s/R | TWINS1 $\eta_{\mathrm{LAD2}}$ Abs. calfactor cts/s/R | TWINS1 $f_{\mathrm{rel,recal}}$ |
|---|---|---|---|
| 20 Jun 2008 | 2.205 | 2.166 | 1.0 |
| 20 Sep 2008 | 2.205 | 2.166 | 1.0 |
| 20 Mar 2010 | 1.03635 | 1.6245 | 1.018 |
| 20 Jun 2010 | 1.21275 | 1.58118 | 0.9778 |

**Table 3.** TWINS2-LAD (absolute and relative $f_{\mathrm{rel,recal}}$) effectivity calibration factors, newly calibrated for 2008 to 2010.

| Date | TWINS2 $\eta_{\mathrm{LAD1}}$ Abs. calfactor cts/s/R | TWINS2 $\eta_{\mathrm{LAD2}}$ Abs. calfactor cts/s/R | TWINS2 $f_{\mathrm{rel,recal}}$ |
|---|---|---|---|
| 20 Jun 2008 | 3.0651 | 1.83633 | 1.018 |
| 20 Sep 2008 | 3.1372 | 3.2144 | 1.023 |
| 20 Mar 2009 | 2.5603 | 3.0454 | 1.011 |
| 20 Sep 2009 | 3.02904 | 3.0771 | 1.006 |

following we will discuss a recalibration method based on exospheric hydrogen Lyman-$\alpha$ intensity profiles under stable solar activity conditions:

Between June–September 2008 the daily geocoronal Lyman-$\alpha$ intensity profiles were measured with the very well calibrated TWINS1 LAD sensors (see Sect. 8). Therefore we will call those profiles "reference profiles" for solar minimum conditions, because we can assume a quite exact knowledge of their Lyman-$\alpha$ intensity values.

For the same seasonal days (i.e. in different years) and under the same solar activity conditions, the geocoronal Lyman-$\alpha$ intensity profiles will not change remarkably. Therefore, the TWINS1 reference profiles can be used as well-known Lyman-$\alpha$ calibration sources for adequate seasonal days and under solar minimum conditions. The reference profiles may have an additional error in their stability or their absolute intensity values, but nevertheless they seemed to be the best sources at the moment we can use to perform the in-flight recalibration of the LAD sensitivity.

In fact, this method is a recalibration of TWINS1/2 LAD data against the reference data of TWINS1 from June–September 2008. There is a cross check criterion, which can prove its correctness: If successfully recalibrated the new absolute LAD sensitivity factors should naturally lead to new relative calibration factors $f_{\mathrm{rel,recal}}$ between LAD1/2 stable at the ideal value of $\approx 1$. This criterion is fulfilled by our method (see Tables 2 and 3).

Stereo observing TWINS1 and TWINS2 spacecraft produces during complete orbits many lines of sight, which either penetrate the H-geocorona in the same (or very nearby) spatial regions or which cross each other. In the mathematical sense, those overlapping or crossing lines of sight represent border conditions in the tomographic enfolding, which constrain the possible solution space in a very effective way. Another constraining factor is the power law dominated geocoronal Lyman-$\alpha$ intensity profile. Despite angular variations of second order the exospheric Lyman-$\alpha$ intensity $I(r)$ value at a given geocentric distance $r$ is in the first order derivable from a power law. At a given time this $r$-dependent power law profile is always very similar and observable from any possible orbital position of a TWINS spacecraft. Therefore it can be used for recalibration purposes. Furthermore, the

Lyman-$\alpha$ intensity power law profile will not change as long as the solar activity conditions are stable.

Based on these arguments we can assume that the well-known "reference power law profiles", as we can provide them from measurements by TWINS1 from 2008, can be used for absolute calibration purposes of other (unknown) calibrated TWINS-data. Mandatory for this practice are an unchanged solar activity and identical seasonal days for the reference and the unkown calibrated Lyman-$\alpha$ intensity profile, respectively. Both conditions are fulfilled in our analysis since the Sun was quite stable at a low activity level until mid-2010 and the TWINS1 reference profiles are available for both (summer-) solstice and (fall-) equinox.

The absolute recalibration procedure itself is an exospheric hydrogen density fit with free fitable LAD sensitivity factors of the unknown calibrated data and constant LAD sensitivity factors of the TWINS1 reference measurements. Mostly overlapping or crossing lines of sight between the reference and the unknown calibrated data will be used for the recalibration as mentioned. As the fit result, the new calibration factors of the LAD with the changed sensitivity for a particular seasonal day of the year are quantified. In this paper this procedure was done to recalibrate TWINS1/2 data for the seasonal conditions (spring- and fall) equinox and summer solstice against the corresponding TWINS1-reference profiles separately. In detail, TWINS1 data from spring equinox and summer solstice of 2010, TWINS2 data from summer solstice 2008, fall equinox 2008 and spring-/fall equinox 2009 were recalibrated against the TWINS1 reference data between June–September 2008 (see Tables 2 und 3).

After the successful determination of the TWINS1/2 absolute LAD-calibration factors, we checked the control criterion concerning their new relative calibration factors $f_{\mathrm{rel,recal}} \approx 1$ between the two sensors LAD1/LAD2 of one spacecraft for spatial overlapping measurements at the actuator turning points. Tables 2 and 3 clearly show that the application of the new absolute calibrations factors results in a very good value of about 1 for the new relative calibration factors $f_{\mathrm{rel,recal}}$.

It became clear that TWINS2 has a factor of roughly 1.5 higher LAD-sensitivity compared to TWINS1. On the other hand, that higher effectivity leads to a shorter lifetime for

the TWINS2 LAD because of the higher detector exhausting rate.

As a methodical test, the absolute calibration procedure was performed with the known exospheric hydrogen distribution from Hodges (1994) and testwise shifted (decalibrated) LAD-sensitivity factors of one satellite. The sensitivity factors of the other satellite were treated as constant. In every test case the method resulted with the correct (unshifted) sensitivity factors of the before testwise-shifted LAD.

## 10   Scattering phase function correction

Brandt and Chamberlain (1959) described an angular intensity dependence $I(\alpha)$ of the scattered Lyman-$\alpha$ photons with respect to the direction of the incoming (solar) Lyman-$\alpha$ photons as follows:

$$I(\alpha) = 1 + \frac{1}{4}\left(\frac{2}{3} - \sin^2(\alpha)\right). \qquad (1)$$

The maximal (percentage) variation of this angular dependence compared to the isotropic case is $+16.7\%$ for $\alpha = 0°$, $180°$ and $-8.3\%$ for $\alpha = 90°$, $270°$. That means, in other words, there is a relatively small preference for forward/backward scattering in the Lyman-$\alpha$ resonant scattering process. We correct our model scattering calculations by the inclusion of the phase function from Eq. (1). Since the numerical corrections due to this phase function are relatively small, our test fits of the neutral exospheric H-density distribution with and without consideration of the phase function show very small quantitative differences.

## 11   Solar conditions

Between June 2008 and October 2009, the solar activity conditions were quite stable and at an extraordinary low level. From October 2009 to June 2010, the solar activity level began to increase slightly but remained on a relatively low level. The total solar Lyman-$\alpha$ flux between June 2008–June 2010 as measured by TIMED SEE and SORCE SOLSTICE calibrated to UARS SOLSTICE level (Woods et al., 2000) (provided by LASP, Laboratory For Atmospheric And Space Physics, University of Boulder, Colorado) is shown in Fig. 6. Additionally, all seasonal days we used in the summer solstice and in the equinox dataset, respectively, are marked as red points in Fig. 6. A maximum flux increase of about 10 % until June 2010 compared to June 2008 was observed together with an increasing level of variability.

In this paper we assume that a 10 % higher solar Lyman-$\alpha$ flux level and its slightly increased variability until June 2010 compared to 2008 is too small to cause remarkable changes of the neutral geocoronal H-density distribution. As a consequence of this assumption, we basically expect to see the
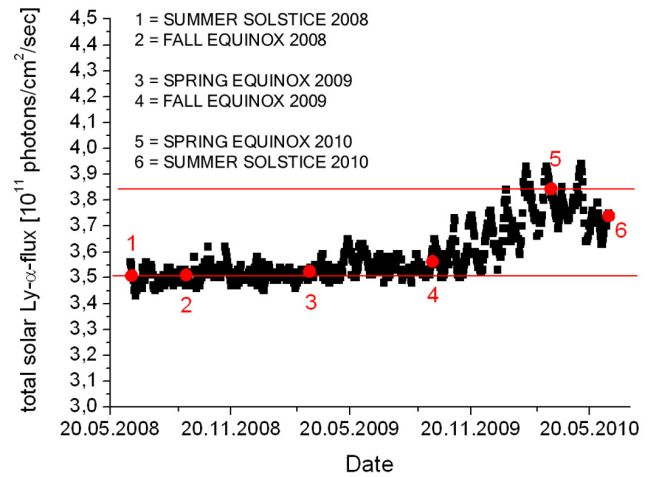


**Fig. 6.** The composite, total solar Lyman-$\alpha$ flux taken from TIMED SEE and SORCE SOLSTICE which shows low flux values and low variability until end of 2009 followed by a 10 % increase until June 2010. Red points mark the dates which are included in the model fit. The 27 day period of solar activity is also visible as small periodic peaks.

same (representative) geocoronal neutral H-density distribution for all three summer-solstice constellations between June 2008 and June 2010 (same for the equinox constellations). The daily fluctuating g-factors caused by the different solar Lyman-$\alpha$ fluxes were, however, considered in the calculations.

The solar 10.7 cm radioflux (taken from NGDC), which is also an index for the solar activity, remains at a low level between June 2008 and June 2010 and was modulated with fluctuations comparable to the solar Lyman-$\alpha$ flux variability.

## 12   Interplanetary Lyman-$\alpha$ background

Due to scattered Lyman-$\alpha$ radiation by the interstellar hydrogen density distribution inside the heliosphere, there exists a background signal, which has to be considered and subtracted in our model. In order to calculate this contribution, we use a hot model of this density distribution (Fahr, 1971; Thomas, 1978). For the incoming flow vector we use the ecliptic longitude $= 252.5°$ and the ecliptic latitude $= 8.8°$ (Lallement et al., 2005) as LISM wind vector coordinates.

The bulk velocity and the temperature is assumed to be $v_0 = 22\,\text{km s}^{-1}$ and $T = 12\,000\,\text{K}$ (Costa et al., 1999). The neutral H-density at the termination shock is adopted to be $n_0 = 0.1\,\text{cm}^{-3}$ (Bzowski et al., 2008).

To take into account the solar influence on the nearby hydrogen density distribution, we use existent databases. In order to calculate the ionization rate by charge exchange, we use the solar wind proton density and velocity as published in the OMNI database (http://cohoweb.gsfc.nasa.gov/form/omni_m.html). The needed charge exchange cross section is
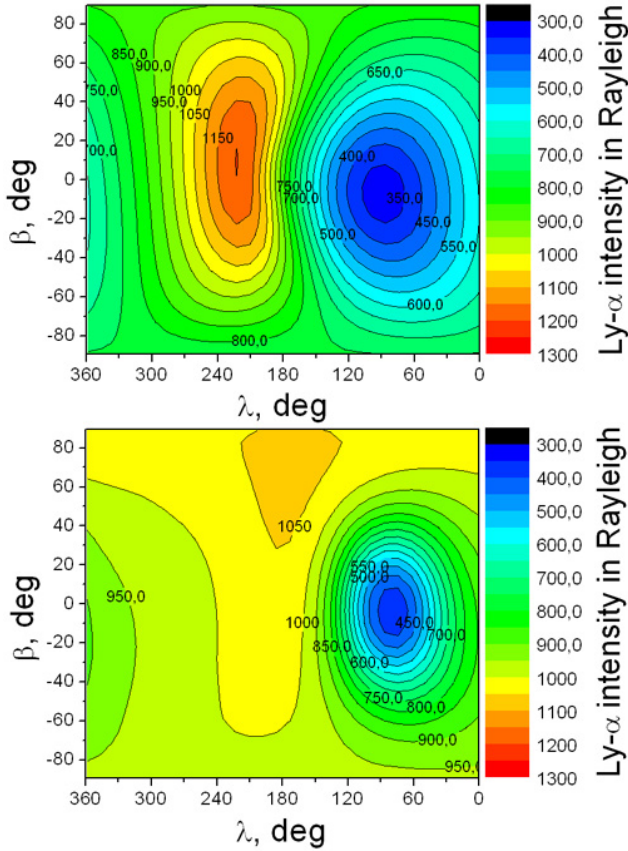
**Fig. 7.** Used interplanetary Lyman-$\alpha$ glow intensity all-sky-maps as calculated with the hot model. Top: 20 September 2009 (fall equinox). Bottom: 20 June 2010 (summer solstice).

taken from Bzowski (2001). The so gained values are then averaged over a period of one year. The latitudinal dependence of this ionization rate is also considered, assuming a sinusoidal variation between the ecliptic and polar ionization rates (Witt et al., 1979). The asymmetry parameter $A$ is assumed to be 0.5 in 2008/2009 and 0.3 in 2010 (Sokol et al., 2012). The ecliptic longitude of the ascending node of the solar equator (J2000) is 75.77°. The inclination of the solar equator to the ecliptic is 7.25°. In order to calculate the EUV ionization rates, we use the F10.7 cm measurements taken from the UK solar system data center (http://www.wdc.rl.ac.uk), average these data over one solar rotation period and then use a proxy correlation function (see Bzowski et al., 2013).

The ratio between the solar radiation pressure force and the gravitational force can be (as usual) calculated by using the solar Lyman-$\alpha$ line center intensity. The total solar Lyman-$\alpha$ flux is taken from the LASP database. After averaging these data over one solar rotation period, we use a proxy function given by Emerich et al. (2005).

The images in Fig. 7 show the interstellar Lyman-$\alpha$ intensity maps for summer solstice 2010 and fall equinox 2009 as an example.

## 13 Mathematical model of the H-Geocorona

As the mathematical model for the neutral terrestrial H-density distribution between 3–10 $R_{\mathrm{E}}$ (within the optically thin regime), the spherical harmonic representation up to a polynomial number $l = 2$ is used:

$$n_{\mathrm{H}}(r, \theta, \phi) = N(r)\sqrt{4\pi} \sum_{l=0}^{2} \sum_{m=0}^{l} Z(r, \theta, \phi) \qquad (2)$$

with

$$Z = [A_{\mathrm{lm}}(r)\cos(m\phi) + B_{\mathrm{lm}}(r)\sin(m\phi)]\, Y_{\mathrm{lm}}(\theta) \qquad (3)$$

where $Y_{\mathrm{lm}}(\theta)$ are the spherical harmonic Legendre-polynomials. This coefficient parameterization is based on the simplified version of the Hodges (1994) model that was employed by Zoennchen et al. (2010) and is also used with some modifications in this work.

The geocoronal coverage in this analysis could be improved tremendously by the involvement of (partly stereo) data from TWINS1 and TWINS2 using LAD-lines of sight from very different orbital positions as described in Sects. 4–6. This improvement makes it possible to allow for fully 3-D angular dependences of both longitude $\phi$ and latitude $\theta$ within the model. As a consequence of that, all coefficients $A_{\mathrm{lm}}$ and $B_{\mathrm{lm}}$ of the spherical harmonic expansion were treated as freely fitable within the model.

Different from Zoennchen et al. (2011), in this work we replaced the $r$-dependence of the $A_{\mathrm{lm}}(r)$- and $B_{\mathrm{lm}}(r)$-coefficients by the natural logarithmic functions

$$A_{\mathrm{lm}} = (a_{\mathrm{lm}} + b_{\mathrm{lm}} \cdot \ln(r)) \times 10^{-4} \qquad (4)$$

$$B_{\mathrm{lm}} = (p_{\mathrm{lm}} + q_{\mathrm{lm}} \cdot \ln(r)) \times 10^{-4} \qquad (5)$$

with constant $A_{00} = 1$. Restoration tests of the Hodges (1994) model based on TWINS1/2 lines of sight brought the result that this logarithmic $r$-dependence of $A_{\mathrm{lm}}(r)$ and $B_{\mathrm{lm}}(r)$ can restore the Hodges (1994) model substantially better than the earlier used linear approach.

To approximate particularly the $N(r)$-term, a power law $N(r) = c \cdot r^{-k}$ function was used (with $r$ as the geocentric distance in $R_{\mathrm{E}}$).

For lower geocentric distances $< 3\,R_{\mathrm{E}}$ (where the H-geocorona turns to be optically thick), we adapted a Chamberlain-like model as described in Sect. 15.
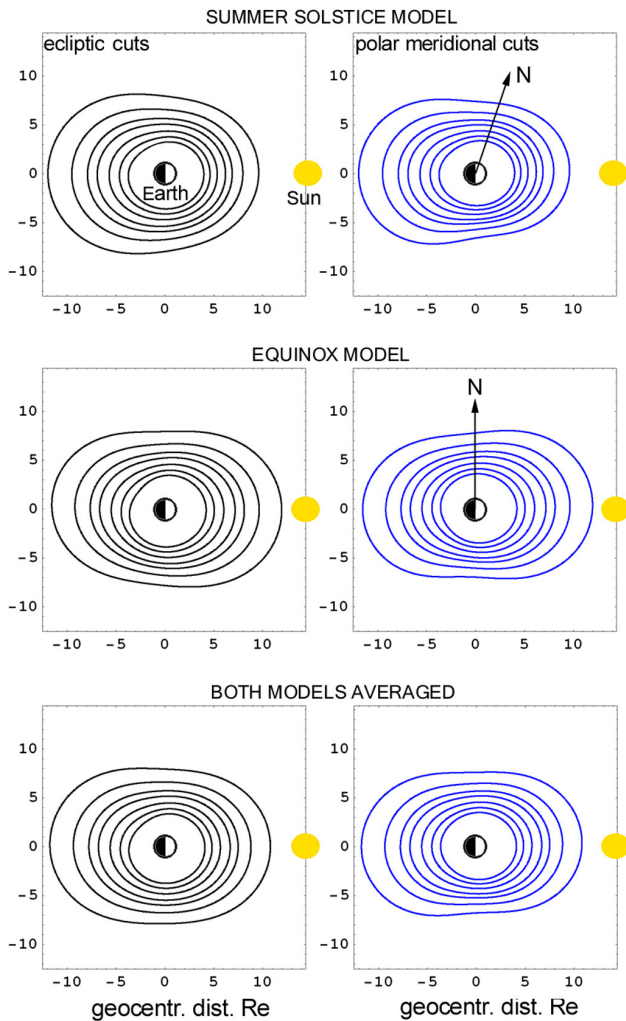
**Fig. 8.** Geocoronal H-density distribution fits for summer solstice (top), equinox (middle) and both averaged (bottom) separately as ecliptic cut (left side) and polar meridional cut (right side). The density contours for all 6 images are from outside to inside: 30, 50, 75, 100, 150, 225, 337 cm$^{-3}$.

**Table 4.** Summer-solstice model fit coefficients.

| $N(r) = c \cdot r^{-k}$ | $c = 10\,172.7$ | $k = 2.70862$ |
|---|---|---|
| $A_{00}(r) = 1$ | always | |
| $A_{10}(r) = a_{10} + b_{10} * \ln(r)$ | $a_{10} = -389.04$ | $b_{10} = 539.94$ |
| $A_{11}(r) = a_{11} + b_{11} * \ln(r)$ | $a_{11} = -7536.18;$ | $b_{11} = 4820.56$ |
| $A_{20}(r) = a_{20} + b_{20} * \ln(r)$ | $a_{20} = 1164.37;$ | $b_{20} = -1593.96$ |
| $A_{21}(r) = a_{21} + b_{21} * \ln(r)$ | $a_{21} = -576.586;$ | $b_{21} = 93.92$ |
| $A_{22}(r) = a_{22} + b_{22} * \ln(r)$ | $a_{22} = -1681.39;$ | $b_{22} = 2335.94$ |
| $B_{11}(r) = p_{11} + q_{11} * \ln(r)$ | $p_{11} = 2756.56;$ | $q_{11} = -1337.19$ |
| $B_{21}(r) = p_{21} + q_{21} * \ln(r)$ | $p_{21} = -1745.40;$ | $q_{21} = 1414.75$ |
| $B_{22}(r) = p_{22} + q_{22} * \ln(r)$ | $p_{22} = 168.51;$ | $q_{22} = 7.758$ |

**Table 5.** Equinox model fit coefficients.

| $N(r) = c \cdot r^{-k}$ | $c = 11\,657.9$ | $k = 2.71619$ |
|---|---|---|
| $A_{00}(r) = 1$ | always | |
| $A_{10}(r) = a_{10} + b_{10} * \ln(r)$ | $a_{10} = -6.075;$ | $b_{10} = 334.16$ |
| $A_{11}(r) = a_{11} + b_{11} * \ln(r)$ | $a_{11} = -2994.08;$ | $b_{11} = 892.39$ |
| $A_{20}(r) = a_{20} + b_{20} * \ln(r)$ | $a_{20} = 1759.70;$ | $b_{20} = -1816.44$ |
| $A_{21}(r) = a_{21} + b_{21} * \ln(r)$ | $a_{21} = 1048.91;$ | $b_{21} = -669.89$ |
| $A_{22}(r) = a_{22} + b_{22} * \ln(r)$ | $a_{22} = -4969.92;$ | $b_{22} = 4281.99$ |
| $B_{11}(r) = p_{11} + q_{11} * \ln(r)$ | $p_{11} = 4110.95;$ | $q_{11} = -2073.98$ |
| $B_{21}(r) = p_{21} + q_{21} * \ln(r)$ | $p_{21} = -728.20;$ | $q_{21} = 528.00$ |
| $B_{22}(r) = p_{22} + q_{22} * \ln(r)$ | $p_{22} = 1230.22;$ | $q_{22} = -766.81$ |

The corresponding fit coefficients of each model fit are listed separately in the following Tables 4 (summer solstice), 5 (equinox) and 6 (seasonal averaged) with $r$ as the geocentric Earth distance in Earth radii $R_E$. The listed $A_{lm}$ and $B_{lm}$ coefficients need to be multiplied with $10^{-4}$ (with the exception of $A_{00}$).

As visible in Fig. 8, the angular structures of the exospheric hydrogen distributions seem to be strongly aligned with the Earth–Sun line. This alignment is manifest in the fit results independent from the season. A cigar-like shape of the density structure (in both cuts) is obvious. This encourages our expectation that the shape of the terrestrial neutral H exosphere is mainly Sun-controlled.

The different angular dependences are discussed in the following Sects. 18–21. The clearly pronounced Earth–Sun line alignment of the geocoronal H-density shape which we found in our fits is different from results published by Bailey and Gruntman (2011) who presented a somewhat tilted shape with respect to the Earth–Sun line (with different tilt angles for the ecliptic cut and the polar meridional cut).

## 14 Model fits for equinox and summer solstice

Based on the two separately assembled TWINS1/2-datasets for the equinox- and the summer-solstice seasons, we fit two separate seasonal neutral exospheric H-density models, which should be representative of the respective seasons under adequate solar minimum conditions. Additionally, these two seasonal models were averaged together into one seasonal-averaged model (in the following called "averaged model").

The fit results for the two seasonal and also the (seasonal) averaged geocoronal H-density distributions are presented as contour plots in Fig. 8 (left images: ecliptic cuts, right images: polar meridional cuts).

## 15 Spherically symmetric model extension for lower distances < 3 $R_E$

For lower geocentric distances (less than 3 $R_E$), the single scattering approach based on optically thin conditions loses its validity as the H-geocorona there tends to be optically thick for resonant Lyman-$\alpha$ scattering. The neutral H-density distribution for those lower distances is approximated by a

**Table 6.** Seasonal averaged model fit coefficients.

| $N(r) = c \cdot r^{-k}$ | $c = 10915.119$ | $k = 2.7126401$ |
|---|---|---|
| $A_{00}(r) = 1$ | always | |
| $A_{10}(r) = a_{10} + b_{10} * \ln(r)$ | $a_{10} = -185.29;$ | $b_{10} = 430.44$ |
| $A_{11}(r) = a_{11} + b_{11} * \ln(r)$ | $a_{11} = -5125.25;$ | $b_{11} = 2735.51$ |
| $A_{20}(r) = a_{20} + b_{20} * \ln(r)$ | $a_{20} = 1481.46;$ | $b_{20} = -1712.69$ |
| $A_{21}(r) = a_{21} + b_{21} * \ln(r)$ | $a_{21} = 288.61;$ | $b_{21} = -312.91$ |
| $A_{22}(r) = a_{22} + b_{22} * \ln(r)$ | $a_{22} = -3430.27;$ | $b_{22} = 3370.85$ |
| $B_{11}(r) = p_{11} + q_{11} * \ln(r)$ | $p_{11} = 3477.09;$ | $q_{11} = -1729.22$ |
| $B_{21}(r) = p_{21} + q_{21} * \ln(r)$ | $p_{21} = -1205.50;$ | $q_{21} = 944.08$ |
| $B_{22}(r) = p_{22} + q_{22} * \ln(r)$ | $p_{22} = 732.60;$ | $q_{22} = -403.69$ |



**Fig. 9.** Longitudinal H-density profiles for $\phi = 0°$-$360°$ at $4R_E$ (left) and $8R_E$ (right) geocentric distance separate for the summer-solstice- (blue), equinox- (red) and seasonal-averaged (gray) model fits.

spherically symmetric (Chamberlain, 1963)-like model:

$$n_H(r) = a \cdot \exp(b/r). \qquad (6)$$

We use this Chamberlain-like model as an extension for $r < 3R_E$ of our spherically harmonic model (Eq. 2). That combined (extended) model provides H-density values from $\approx 1000$ km altitude up to $10 R_E$ geocentric distance. In order to get a (nearly) continuous H-density interface between the two models at $r = 3R_E$, we fit the Chamberlain-like model coefficients $a$ and $b$ to

$$a = 32.745 \quad ; \qquad b = 8.3845 . \qquad (7)$$

The used two fit constraints are an H-density value at $1R_E$, as published by (Carruthers et al., 1976), and the spherically symmetric averaged H-density value from our seasonally averaged model at the interface geocentric distance of $3R_E$.

The H-density profile fit of the Chamberlain-like model and its adaption to our averaged spherical harmonic extension model profile at $3R_E$ is shown in Fig. 14 in segment (A).

## 16 Interpolation of a daily H-density distribution for quiet solar minimum conditions

Since the geocoronal H-density distribution is changing periodically between the seasonal equinox and solstice, it seems to be reliable to calculate the H-density distribution for a particular day of the year by an (linear and time weighted) interpolation of the two seasonal H-density distributions where this day is situated in between.

In Sect. 14 we present neutral geocoronal H-density fits for equinox and summer solstice separately. Since we do not have reliable winter-solstice data from TWINS between June 2008 and June 2010, we assume, instead, that the winter-solstice model is a z-axis inverted summer-solstice H-density model, which was also practiced by Hodges (1994). Using this assumption a winter-solstice model for solar quiet conditions can be easily calculated from our summer-solstice model doing a z-axis inversion.

From that point all the neccessary seasonal equinox, summer- and winter solstices are known and a geocoronal
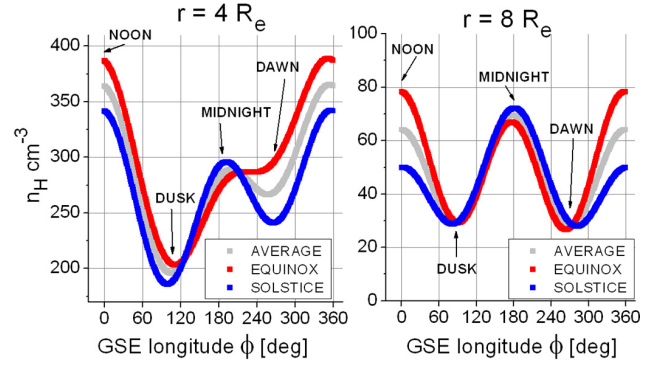
H-density model can be interpolated for each day of the year, as long as the solar activity level is still low and stable.

## 17 Angular H-density dependences

For different geocentric distances $r$, the neutral geocoronal H-density distribution is mainly dominated by a power law decrease. In comparison to that strongly monotonically falling function over $r$, the angular dependences of the H-geocorona seem to be quantitatively small.

Nevertheless, different longitudinal and latitudinal dependences of the neutral geocoronal H-density distribution exist and could be clearly found in our two seasonal model fits. The fit results suggest a cigar-like shaped neutral exospheric H-density structure aligned along the Earth–Sun line.

The main angular features are the noon/dusk-asymmetry in the ecliptic plane, the dayside/nightside-asymmetry, the H-density depletion over North- and South Pole and the dawn/dusk-asymmetry. These features are described in more detail in the following Sects. 18–21.

Figures 9 and 10 show the $\phi$- and $\theta$-profiles for two particular geocentric distances $4R_E$ and $8R_E$ separately for our equinox-, summer-solstice and the seasonally-averaged model fit.

Interestingly, both seasonal fits show a longitudinal deviation of their maximum dayside density of about $-5°$ with respect to the solar direction (see Fig. 9). This might be due to the aberration of the solar wind caused by the Earth's orbit around the Sun and is therefore interpretable as a sign for influences of enhanced hydrogen densities between bow shock and magnetopause to the exosphere below. Since many of the dayside LOS are lost due to solar stray light, that small deviation may also be an observational effect.
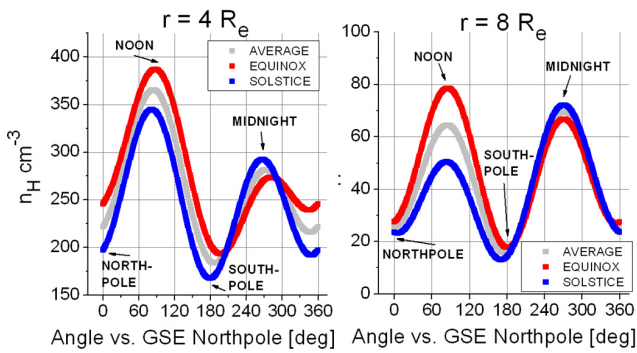
**Fig. 10.** Latitudinal H-density profiles for $\theta = 0$–$180°$ (North Pole to South Pole over noon) and $\theta = 180$–$360°$ (South Pole to North Pole over midnight) at $4\,R_{\mathrm{E}}$ (left) and $8\,R_{\mathrm{E}}$ (right) geocentric distance separate for the summer-solstice- (blue), equinox- (red) and seasonal-averaged (gray) model fits.

## 18  Noon/dusk and noon/dawn asymmetry

As one of the most obvious angular features within the ecliptic plane we found significant larger noon H-densities compared to the corresponding values at dusk or dawn side. This asymmetry can be directly seen in the ecliptic cuts (left side) of Fig. 8 for both seasonal fits and also within the longitudinal profiles in Fig. 9. The effect is quantitatively among the strongest angular dependencies of the neutral H-geocorona which we found. It increases with geocentric distance $r$ and appears stronger for the equinox compared to summer solstice.

Taken from the seasonal averaged fit, the noon/dusk density ratio value is 1.8 at $4\,R_{\mathrm{E}}$ and even larger with $> 2.2$ at $8\,R_{\mathrm{E}}$. Since H-densities at dusk seemed to be lower than at dawn (see Sect. 21), the effect is more visible in the noon/dusk-ratio compared to the noon/dawn-ratio (see Fig. 9). The explanation of that asymmetry effect is currently under investigation.

## 19  Dayside/nightside asymmetry

Within the ecliptic plane, the noon side differs from the midnight side. In particular, for geocentric distances $r > 6\,R_{\mathrm{E}}$ (for summer solstice) and $r > 8$–$9\,R_{\mathrm{E}}$ (for equinox), respectively, the midnight H-densities tend to be larger than the corresponding noon H-densities (see Fig. 8).

This effect is qualitatively in good agreement with the behavior of the H-geotail-like phenomenon as reported by Østgaard et al. (2003). The seasonal comparison of the H-geotail-like structure in our fits leads to the result, that the effect becomes visible at lower distances at summer solstice (starting at $6\,R_{\mathrm{E}}$) compared to the equinox situation (starting at $\approx 8$–$9\,R_{\mathrm{E}}$) (see also the longitudinal profile at $8\,R_{\mathrm{E}}$ in Fig. 9).

A possible physical contribution to this phenomena may be a more efficient transport process of energetic neutral H-atoms from the dayside to the nightside at solstice. Those energetic neutral H-atoms are created from solar wind protons by charge exchange reactions with cold geocoronal H-atoms near the Earth magnetopause.

Particularly the exospheric nightside Lyman-$\alpha$ intensities may need some corrections due to the optically thin approximation used in this paper.

## 20  Neutral H-density depletion over the North- and South Pole

Compared to the neutral geocoronal H-density at the day side (i.e. at noon), the corresponding values over the North- and South Pole of the Earth are depleted. This effect was predicted by the Hodges (1994) model and also reported by Bailey and Gruntman (2011). The improved coverage per dataset in this work now allows a more reliable reconstruction of the neutral H-density depletion over the terrestrial polar regions.

The degree of the depletion increases with geocentric distance $r$ and appears comparable for both Earth poles. The depletion effect seems to be a little bit weaker for the North Pole compared to the South Pole. Since both TWINS1/2 satellites only observe from north towards south, the Northern Hemisphere is far better covered than the Southern. Therefore, this small density depletion difference between North- and South Pole may be an observational effect.

The latitudinal neutral H-density profiles at $4\,R_{\mathrm{E}}$ and $8\,R_{\mathrm{E}}$ are shown in Fig. 10. The seasonal averaged H-density North Pole/noon-ratio is 0.62 at $4\,R_{\mathrm{E}}$ and even smaller with 0.39 at $8\,R_{\mathrm{E}}$. The polar depletion effect is stronger for equinox compared to the summer solstice situation.

Mainly responsible for the polar regional neutral H-density depletion are enhanced charge exchange- and ionization reactions within the polar wind region and the increased inflow of charged, energetic particles within the Earth magnetic cusp region. Further investigation is needed to explain this effect quantitatively.

## 21  Dawn/dusk asymmetry

We found a significantly larger geocoronal H-density at the Earth morning side (dawn) compared to the evening side (dusk) for geocentric distances between 3–$8\,R_{\mathrm{E}}$. This effect is clearly seen in both seasonal model fits and is stronger pronounced at equinox compared to summer solstice. Very interesting is the fact that the asymmetry decreases for larger geocentric distance $r$ and will practically vanish beyond $\approx 8\,R_{\mathrm{E}}$.

Taken from the seasonal averaged fit, the ecliptic H-column densities along LOS from 3–$10\,R_{\mathrm{E}}$ for longitudinal angles $\phi$ from dusk ($90°$) over midnight ($180°$) towards dawn ($270°$) were calculated and are presented in Fig. 11. The dawn/dusk H-column density ratio of $\approx 1.25$–$1.3$ is
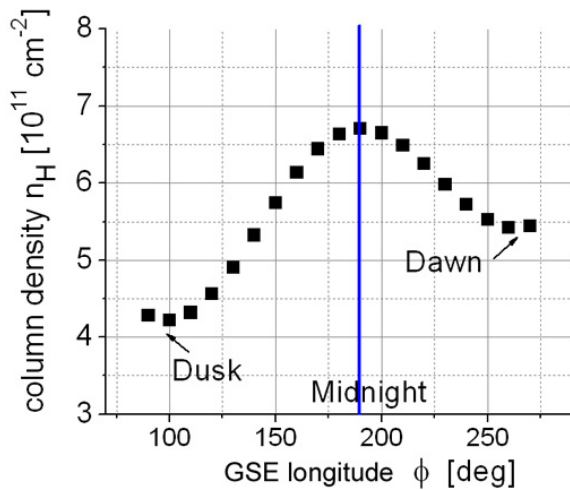
**Fig. 11.** Dawn/dusk asymmetry of the H-column densities (between 3–10 $R_E$) for longitudinal angles $\phi = 90$–$270°$ taken from the seasonal averaged model fit.



**Fig. 12.** TWINS1/2 equinox and summer-solstice dataset LAD-Lyman-$\alpha$ intensities in Rayleigh (black) in comparison to calculated Lyman-$\alpha$ intensities from the Hodges (1994) H-density model ($F_{10.7\text{cm}} = 80$ [$10^{-22}\,\text{W}\,\text{m}^{-2}\,\text{Hz}^{-1}$]).

equivalent to the same dawn/dusk Lyman-$\alpha$ intensity ratio (optically thin regime).

Interesting is the fact that a very similar behavior was published by Mierkiewicz et al. (2012) using a different, ground-based Balmer $\alpha$ observation method to find the H-column densities along lines of sight towards dusk and dawn from the night side of the Earth. The Balmer $\alpha$ resonant scattering intensity of a line of sight is in the first order also proportional to its neutral H-column density. Mierkiewicz et al. (2012) report a 20 % brighter Balmer $\alpha$ intensity of the morning side compared to the evening side. Their value can be transformed into a dawn/dusk H-column density ratio of about 1.2, which is in very good agreement with our result.

The neutral H-density model fit published by Bailey and Gruntman (2011) shows the opposite effect of a roughly 25 % larger dusk-value compared to the dawn-value. This perhaps might have to do with a less complete geocoronal data coverage in their analysis.

Taken from the Hodges (1994) model at exobase heights (480 km), the neutral H-density ratio $n(\text{exobase})_{\text{dawn}}/n(\text{exobase})_{\text{dusk}}$ has a value of about 2.9 under solar quiet conditions. With increasing geocentric distances that ratio decreases for the [Hodges, 1994] model very fast and has nearly vanished for geocentric distances $r \geq 2.5\,R_E$. Different from Hodges (1994), both ratios of our seasonal TWINS-model fits decrease much slower with geocentric distance. As visible in Fig. 9, our seasonal TWINS-model fits show dawn/dusk H-density ratio of 1.4 (equinox) respective 1.35 (solstice) at $r = 4\,R_E$ and still remarkable values up to larger geocentric distances between 4 and 8 $R_E$.

That may indicate the existence of an additional process that transports neutral H-atoms from lower exobase heights ($\approx 500$ km) along eccentric elliptic orbits up to much higher
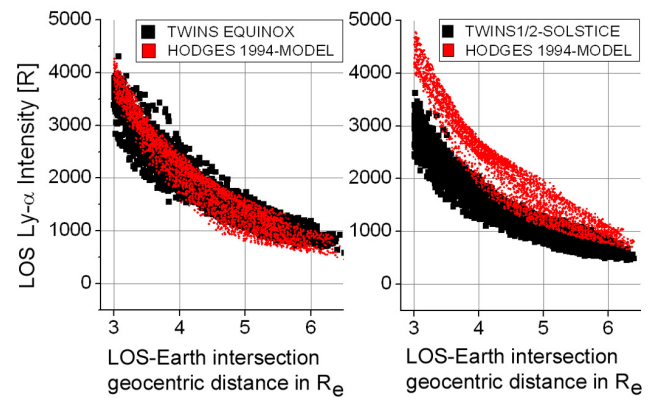
orbital regions. At larger geocentric distances of $r \geq 4\,R_E$, hydrogen atoms of the so-called "elliptic" type may be the dominant contributors to the exospheric H-density (Fahr and Shizgal, 1983; Richter et al., 1979). Elliptic- or satellite-type particles are injected into their orbits above the exobase and can orbit Earth several times without undergoing collisions. Since those orbits most likely are very eccentric, the orbiting H-atoms due to slowest orbital motion can be found with the highest probability near their orbital apogee positions. This causes a pronounced H-density enhancement near their apogee regions, which is in fact most likely opposite to their injection points (near the perigees). The TWINS LAD observed dawn/dusk-asymmetry at $r > 3\,R_E$ may be a sign for a more efficient injection to the relevant elliptic orbits near the dusk exobase compared to the dawn exobase.

It is nevertheless very encouraging to look for the explanation of the observed dawn/dusk H geocoronal asymmetry as given in terms of the above mentioned transport process.

## 22 Seasonal effects compared to Hodges (1994)

These presented seasonal neutral exospheric H-density fits for equinox and summer solstice can be compared to the corresponding seasonal models for low solar activity by Hodges (1994).

For the equinox, the TWINS LAD data and our fit results, respectively, compared to the equinox- (Hodges, 1994) model are in good agreement. This can be seen in Fig. 12 (left plot), where the TWINS1/2 measured Lyman-$\alpha$ intensity profile (black) is plotted against the intensity profile as predicted by the equinox- (Hodges, 1994) model (red). Additionally, in Fig. 13 the radial H-density profile of our equinox model fit (black) is plotted together with the profile of the equinox- (Hodges, 1994) model (dark blue). Both H-density profiles correspond very well.
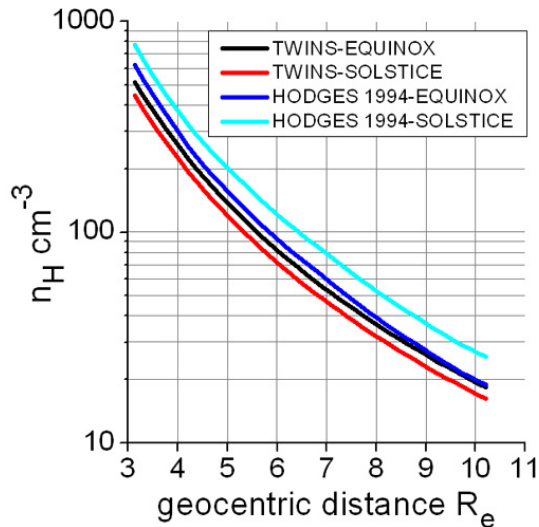
**Fig. 13.** Radial profiles of TWINS equinox model (black) and the equinox (Hodges, 1994) model (blue) are in good agreement. Discrepancies of the the radial profiles of TWINS solstice model (red) and the solstice (Hodges, 1994) model (cyan) are visible.



**Fig. 14.** Segment (A) shows the Chamberlain-like H-density extension for $< 3\,R_{\mathrm{E}}$; segment (B) radial H-density profiles from different models in comparison for $r$ between 3–10 $R_{\mathrm{E}}$.

For the summer solstice the situation is a little different. In that case the solstice (Hodges, 1994) profile shows larger Lyman-$\alpha$ intensities compared to those measured by TWINS1/2 (see Fig. 12, right plot). Hodges (1994) predicts within his model a somewhat denser neutral H exosphere at summer solstice compared to equinox, which we cannot confirm from TWINS observations and our analysis results so far. The solstice (Hodges, 1994) model contains $\approx$ 20–25 % more neutral H-atoms in total (between 3–10 $R_{\mathrm{E}}$) compared to the equinox (Hodges, 1994) model. Different from that is the H-atom number in our solstice-model fit $\approx$ 10 % less than in our equinox-model fit. This discrepancy can be seen in Fig. 12 (right plot) and is also obvious by comparing both radial density profiles as shown in Fig. 13 (our TWINS solstice model = red; the Hodges (1994) solstice model = cyan).

## 23 Comparison with other models

Segment (B) in Fig. 14 shows the comparison of our (seasonal-averaged) TWINS1/2 radial H-density profile with radial profiles of 4 other density models (within the optically thin regime for geocentric distances between 3–10 $R_{\mathrm{E}}$). As visible from Fig. 14, our (seasonal-averaged) model profile is in best agreement with the profiles from Østgaard et al. (2003) and Rairden et al. (1986). The two profiles from Bailey and Gruntman (2011) and Zoennchen et al. (2011) are reasonably close as well. The neutral H-density from our seasonal-averaged model at the subsolar point at 10 $R_{\mathrm{E}}$ is with 18 cm$^{-3}$ close to the value of 4–11 cm$^{-1}$ found with a different method (using IBEX-ENA- and Cluster3-proton data) by Fuselier et al. (2010).
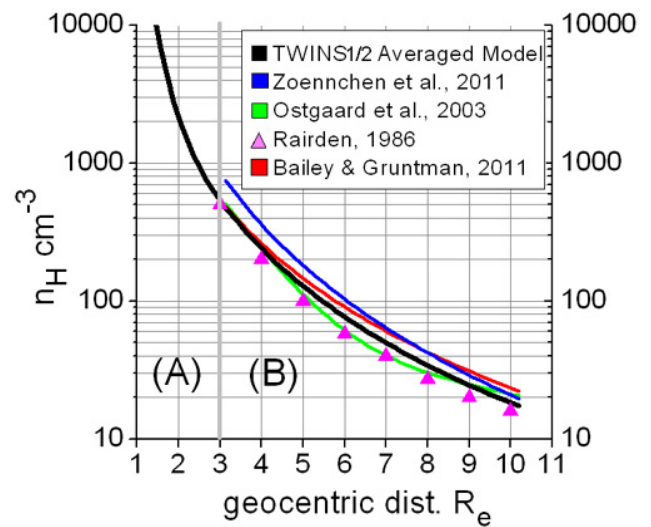
Segment (A) in Fig. 14 shows the radial symmetric extension of our model towards lower geocentric distances $< 3\,R_{\mathrm{E}}$ using a best-fit Chamberlain-like model as described in Sect. 15.

For a particular geocentric distance of 5 $R_{\mathrm{E}}$ we compared our (ecliptic) H-densities for solar zenith angles $\phi$ between 90° (dusk) and 180° (midnight) with the solar zenith angle profiles published by Østgaard et al. (2003) and calculated from the model published by Bailey and Gruntman (2011) (see Fig. 15). The H-density was normalized to 1 at $\phi = 90°$. Our seasonal-averaged model profile and the profile by Østgaard et al. (2003) both increase from dusk to midnight in a similar way. The solar zenith profile calculated from the model by Bailey and Gruntman (2011) shows, however, a different behavior with a H-density decrease from 90° to 180°.

## 24 Range of validity (distance, solar activity, time)

**Valid distances – from geocentric distance between 3–8 $R_{\mathrm{E}}$:** The fits were done using TWINS1/2 LAD lines of sight with geocentric intersection distances larger than 3 $R_{\mathrm{E}}$ in order to be able to use the optically thin approximation. A Chamberlain-like density model for the lower regions, as described in Sect. 15, was used to present an adapted (spheric symmetric) model extension for lower altitude regions down to 1000 km.

**Valid solar conditions – quiet, solar minimum conditions ($\mathbf{F_{10.7cm} < 100}$):** The fits were done using data from the solar minimum with solar radio fluxes $F_{10.7cm} < 100$ between summer solstice 2008 and summer solstice 2010 and should be used only in situations with comparably low solar activity.
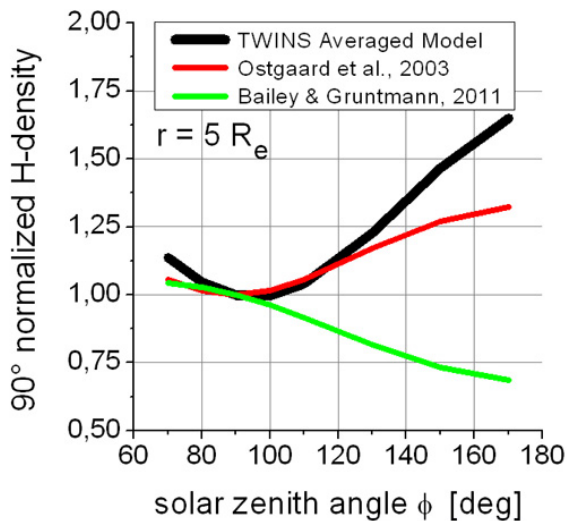
**Fig. 15.** Seasonal averaged TWINS H-density profile (black) at 5 $R_E$ from 90° (dusk) to 180° (midnight) in comparison to Østgaard et al. (2003) (red) and Bailey and Gruntman (2011) (green).

**Valid time frame of use – June 2008 to June 2010:**
Low solar activity with total, solar Lyman-$\alpha$ fluxes comparable to values between 3.5–3.85 [$10^{11}$ photons cm$^2$ s$^{-1}$] of the analysis period June 2008–June 2010.

## 25   Conclusions

Compared to our earlier results (Zoennchen et al., 2010, 2011), this paper presents an extended tomographic Lyman-$\alpha$ analysis of the exospheric hydrogen distribution under solar minimum conditions. For the first time (partly simultaneous) Lyman-$\alpha$ measurements from both of the satellites TWINS1 and TWINS2 during the period from June 2008 to June 2010 were used. Since during that period the solar radiation conditions were relatively constant and prevailed under stable minimum conditions, a nearly constant geocoronal hydrogen exosphere could be expected for identical seasonal days. This allowed us to collect TWINS1/2-data of (spring and fall) equinox and summer solstice from different years in two seasonal-combined datasets, leading to a significantly increased spatial coverage of the exosphere.

Based on these seasonal-combined databases, two typical exospheric hydrogen density distributions for summer solstice and equinox conditions were derived. For both of these seasonal conditions we found the density distributions well aligned with the Earth–Sun line with a small longitudinal deviation of about −5° upsun. This deviation might be due to the aberration effect caused by the Earth's orbit around the Sun. In addition we found significant density depletions over the Earth magnetic poles which slightly differ seasonally. Also, noon densities are greater by up to a factor of 2

compared to the dawn and dusk densities. On the night side, evidence for a geotail-like structure with increased density compared to noon was found pronounced at geocentric distances between 6–8 $R_E$.

Most remarkably, a dawn–dusk density asymmetry with 1.3 higher H-densities on the dawn side was discovered. The expectable dawn-to-dusk density ratio at exobasic heights (see Hodges, 1994) was found to be more strongly pronounced at larger heights (3 to 8 $R_E$) where H-atoms on elliptic orbits start dominating the local exospheric hydrogen densities. The effect decreases with increasing geocentric distance. As a possible explanation we present an orbital transportation effect, where satellite H-atoms might be more effectively injected into circumterrestrial orbits on the dusk side than on the dawn side and then form a more pronounced density near their (opposite situated) apogee regions.

## References

Bailey, J. and Gruntman, M.: Experimental study of exospheric hydrogen atom distributions by Lyman-$\alpha$ detectors on the TWINS mission, J. Geophys. Res., 116, A09302, doi:10.1029/2011JA016531, 2011.

Bishop, J.: Analytic exosphere models for geocoronal application, Planet. Space Sci., 39, 885–893, 1991.

Brandt, J. C. and Chamberlain, J. W.: Hydrogen Radiation in the Night Sky, Astrophysical Journal, 130, 670–682, doi:10.1086/146756, 1959.

Bzowski, M.: A model of Charge Exchange of Interstellar Hydrogen on a Time-Dependent, 2D Solar Wind, Space Sci. Rev., 97, 379–383, 2001.

Bzowski, M., Möbius, E., Tarnopolski, S., Izmodenov, V., and Gloeckler, G.: Density of neutral interstellar hydrogen at the termination shock from Ulysses pickup ion observations, Astron. Astrophys., 491, 7–19, 2008.

Bzowski, M., Sokol, J. M., Tokumaru, M., Fujiki, K., Quemerais, E., Lallement, R., Ferron, S., Bochsler, P., and McComas D. J.: Solar parameters for modeling interplanetary background, Chapter 3 in "Cross-Calibration of Past and Present Far UV Spectra of Solar System Objects and the Heliosphere", ISSI Scientific Report No. 12, edited by: Bonnet, R. M., Quemerais, E., and Snow, M., Springer, in press (astro-ph/1112.2967 v1), 2013.

Carruthers, G. R., Page, T., and Meier, R. R.: Apollo 16 Lyman alpha imagery of the hydrogen geocorona, J. Geophys. Res., 81, 1664–1672, 1976.

Chamberlain, J. W.: Planetary coronae and atmospheric evaporation, Planet. Space Sci., 11, 901–960, 1963.

Costa, J., Lallement, R., Quemerais, E., Bertaux, J. L., Kyrölä, E., and Schmidt, W.: Heliospheric interstellar H temperature from SOHO/SWAN H cell data, Astron. Astrophys., 349, 660–672, 1999.

Emerich, C., Lemaire, P., Vial, J.-C., Curdt, W., Schühle, U., and Wilhelm, K.: A new relation between the central spectral solar H I Lyman a irradiance and the line irradiance measured by SUMER/SOHO during the cycle 23, Icarus, 178, 429–433, doi:10.1016/j.icarus.2005.05.002, 2005.

Fahr, H. J.: The Interplanetary Hydrogen Cone and its Solar Cycle Variations, Astron. Astrophys., 14, 263–274, 1971.

Fahr, H. J. and Shizgal, B.: Modern Exospheric Theories and Their Observational Relevance, Rev. Geophys. Space Phys., 21, 75–124, 1983.

Fuselier, S. A., Funsten, H. O., Heirtzler, D., Janzen, P., Kucharek, H., McComas, D. J., Moebius, E., Moore, T. E., Petrinec, S. M., Reisenfeld, D. B., Schwadron, N. A., Trattner, K. J., and Wurz, P.: Energetic neutral atoms from the Earth's subsolar magnetopause, Geophys. Res. Lett., 37, L13101, doi:10.1029/2010GL044140, 2010.

Hodges Jr., R. R.: Monte Carlo simulation of the terrestrial hydrogen exosphere, J. Geophys. Res., 99, 23229–23247, 1994.

Johnson, F. S.: The Distribution of Hydrogen in the Telluric Hydrogen Corona, Astrophys. Journal, 133, 701, 1961.

Kupperian, J. E., Byram, E. T., Chubb, T. A., and Friedman, H.: Far ultra-violet radiation in the night sky, Planet. Space Sci., 13, doi:10.1016/0032-0633(59)90015-7, 1959.

Lallement, R., Quemerais, E., Bertaux, J. L., Ferron, S., Koutroumpa, D., and Pellinen, R.: Deflection of the Interstellar Neutral Hydrogen Flow Across the Heliospheric Interface, Science, 307, 1447–1449, 2005.

McComas, D. J., Allegrini, F., Baldonado, J., Blake, B., Brandt, P. C., Burch, J., Clemmons, J., Crain, W., Delapp, D., Demajistre, R., Everett, D., Fahr, H., Friesen, L., Funsten, H., Goldstein, J., Gruntman, M., Harbaugh, R., Harper, R., Henkel, H., Holmlund, C., Lay, G., Mabry, D., Mitchell, D., Nass, U., Pollock, C., Pope, S., Reno, M., Ritzau, S., Roelof, E., Scime, E., Sivjee, M., Skoug, R., Sotirelis, T. S., Thomsen, M., Urdiales, C., Valek, P., Viherkanto, K., Weidner, S., Ylikorpi, T., Young, M., and Zoennchen, J.: The two wide-angle imaging neutral-atom spectrometers (TWINS)NASA mission-of- opportunity, Space Sci. Rev., 142, 157, doi:10.1007/s11214-008-9467-4, 2009.

Mierkiewicz, E. J., Roesler, F. L., and Nossal, S. M.: Observed seasonal variations in exospheric effective temperatures, J. Geophys. Res., 117, A06313, doi:10.1029/2011JA017123, 2012.

Nass, H. U., Zoennchen, J. H., Lay, G., and Fahr, H. J.: The TWINS-LAD mission: Observations of terrestrial Lyman-? fluxes, Astrophys. Space Sci. Trans., 2, 27–31, doi:10.5194/astra-2-27-2006, 2006.

Østgaard, N., Mende, S. B., Frey, H. U., Gladstone, G. R., and Lauche, H.: Neutral hydrogen density profiles derived from geocoronal imaging, J. Geophys. Res. Space Phys., 108, 18-1, 2003.

Rairden, R. L., Frank, L. A., and Craven, J. D.: Geocoronal imaging with Dynamics Explorer, J. Geophys. Res., 91, 13613–13630, 1986.

Richter, E., Fahr, H. J., and Nass, H. U.: Satellite particle exospheres of planets – Application to earth, Planet. Space Sci., 27, 1163–1173, doi:10.1016/0032-0633(79)90136-3, 1979.

Sokol, J. M., Bzowski, M., Tokumaru, M., Fujiki, K., and McComas, D. J.: Heliolatitude and Time Variations of Solar Wind Structure from in situ Measurements and Interplanetary Scintillation Observations, Solar Physics, Online First, 05/2012, doi:10.1007/s11207-012-9993-9, 2012.

Thomas, G. E.: The interstellar wind and its influence on the interplanetary environment, Annual review of earth and planetary sciences, 6, (A78-38764 16-42) Palo Alto, Calif., Annual Reviews, Inc., 1978, 173–204, 1978.

Thomas, G. E. and Bohlin, R. C.: Lyman-alpha measurements of neutral hydrogen in the outer geocorona and in interplanetary space, J. Geophys. Res., 77, 2752–2761, 1972.

Witt, N., Blum, P. W., and Ajello, J. M.: Solar wind latitudinal variations deduced from Mariner 10 interplanetary H /1216 A/ observations, Astron. Astrophys., 73, 272–281, 1979.

Woods, T. N., Tobiska, W. K., Rottman, G. J., and Worden, J. R.: Improved solar Lyman alpha irradiance modeling from 1947 through 1999 based on UARS observations, J. Geophys. Res., 105, 27195–27215, doi:10.1029/2000JA000051, 2000.

Zoennchen, J. H.: Modellierung der dreidimensionalen Dichteverteilung des geokoronalen Neutralwasserstoffes auf Basis von TWINS Ly-Alpha-Intensitaetsmessungen, Phd thesis, URN: urn:nbn:de:hbz:5N-08886, available at: http://www.ulb.uni-bonn.de/, 2006.

Zoennchen, J. H., Nass, U., Lay, G., and Fahr, H. J.: 3-D-geocoronal hydrogen density derived from TWINS Ly-?-data, Ann. Geophys., 28, 1221–1228, doi:10.5194/angeo-28-1221-2010, 2010.

Zoennchen, J. H., Bailey, J. J., Nass, U., Gruntman, M., Fahr, H. J., and Goldstein, J.: The TWINS exospheric neutral H-density distribution under solar minimum conditions, Ann. Geophys., 29, 2211–2217, doi:10.5194/angeo-29-2211-2011, 2011.